Pharm Res (2014) 31:3085–3094
DOI 10.1007/s11095-014-1401-8

RESEARCH PAPER

NanoXCT: A Novel Technique to Probe the Internal Architecture of Pharmaceutical Particles

Jennifer Wong • Dexter D'Sa • Matthew Foley • John Gar Yan Chan • Hak-Kim Chan

Received: 10 March 2014 / Accepted: 28 April 2014 / Published online: 28 May 2014

ABSTRACT

Purpose To demonstrate the novel application of nano X-ray computed tomography (NanoXCT) for visualizing and quantifying the internal structures of pharmaceutical particles.

Methods An Xradia NanoXCT-100, which produces ultra high-resolution and non-destructive imaging that can be reconstructed in three-dimensions (3D), was used to characterize several pharmaceutical particles. Depending on the particle size of the sample, NanoXCT was operated in Zernike Phase Contrast (ZPC) mode using either: 1) large field of view (LFOV), which has a two-dimensional (2D) spatial resolution of 172 nm; or 2) high resolution (HRES) that has a resolution of 43.7 nm. Various pharmaceutical particles with different physicochemical properties were investigated, including raw (2-hydroxypropyl)-beta-cyclodextrin (HβCD), poly (lactic-co-glycolic) acid (PLGA) microparticles, and spray-dried particles that included smooth and nanomatrix bovine serum albumin (BSA), lipid-based carriers, and mannitol.

Results Both raw HβCD and PLGA microparticles had a network of voids, whereas spray-dried smooth BSA and mannitol generally had a single void. Lipid-based carriers and nanomatrix BSA particles resulted in low quality images due to high noise-to-signal ratio. The quantitative capabilities of NanoXCT were also demonstrated where spray-dried mannitol was found to have an average void volume of $0.117 \pm 0.247\ \mu m^3$ and average void-to-material percentage of 3.5%. The single PLGA particle had values of $1993\ \mu m^3$ and 59.3%, respectively.

Conclusions This study reports the first series of non-destructive 3D visualizations of inhalable pharmaceutical particles. Overall, NanoXCT presents a powerful tool to dissect and observe the interior of pharmaceutical particles, including those of a respirable size.

J. Wong • D. D'Sa • J. G. Y. Chan • H.-K. Chan (✉)
Advanced Drug Delivery Group, Faculty of Pharmacy
University of Sydney Camperdown, NSW 2006, Australia
e-mail: kim.chan@sydney.edu.au

M. Foley
Australian Center for Microscopy & Microanalysis, University of Sydney
Camperdown, NSW 2006, Australia

KEY WORDS Inhalation aerosols · NanoCT · Porous particles · Pulmonary drug delivery · X-ray computed tomography

INTRODUCTION

Porous particles continue to be an attractive particle engineering approach to enhance aerosol performance of pharmaceutical powders (1, 2). In dry powder inhalers (DPIs), porous particles can achieve emitted doses as high as 96% and respirable fractions up to 92% (3), whereas in pressurized metered dose inhalers (pMDIs) such particles impart better physical stability, content uniformity and aerosolization efficiency (4). Reasons for these properties could be due to reduced Van der Waals forces as well as lower aerodynamic diameters, by virtue of trapped air volume. For spherical particles, the aerodynamic diameter (d_a) can be calculated using the equation.

$$d_a = d_p\sqrt{\frac{\rho}{\rho o}} \tag{1}$$

where d_p is the geometric diameter, ρ is the particle density, and ρ_0 the unit density (*i.e.* 1 g/cm^3) (5).

Since this relationship has been demonstrated experimentally (6), studying the interior of particles will give important insight into their aerodynamic behavior. For example, a study by Chew *et al.* (7) found that a slight increase in surface corrugation significantly enhanced fine particle fraction (FPF) from 27% to 41%. However, further increase in corrugation showed little improvement in FPF. Later, Heng *et al.* (8) suggested that this lack of improvement in aerosol performance of corrugated BSA (compared to smooth BSA) may be due to these corrugated particles being solid (instead of hollow). Otherwise, these corrugated particles would be expected to have a smaller aerodynamic diameter and hence higher respirable fractions.

Advanced microscopic techniques used to probe the internal structures of particles have included transmission electron

microscopy (TEM), confocal laser scanning microscopy (CLSM), scanning electron microscopy (SEM), and more recently focused-ion beam-SEM (FIB-SEM). Chew & Chan (9) examined the interior of individual spray-dried mannitol by a freeze-fracture procedure. The freeze-fractured surface was replicated in carbon and then viewed under TEM. The same authors (10) later characterized the interior of spray-dried bovine serum albumin (BSA) using CLSM. Powders were fixed to a glass slide and continuous sectioning along the z-axis of the sample attempted to identify voids. Interestingly, FIB-SEM revealed hollow interiors in particles where previous techniques had failed (9, 10). Although FIB-SEM has become a popular approach to study particle porosity (11, 12), potential artifacts that can affect the sample include heat damage, gallium implantation and changing crystal structure (13–15). FIB-milled material may also redeposit on the exposed surfaces of the porous structure, which can confuse observers (16). Apart from the possibility to introduce artifacts, current methods are also limited by tedious sample preparation and their destructive nature. Furthermore, data obtained by such methods are only in two dimensions (2D), surface specific, and remain largely qualitative. Therefore, there is a need for a non-destructive method (17) that can address these limitations. X-ray computed tomography (XCT) introduces minimal artifacts and presents a useful complementary technique for investigating the internal structures of pharmaceutical particles.

XCT is an imaging technique where individual projections recorded from different angles are used to reconstruct the internal structure of a sample of interest. It offers extensive and non-destructive imaging that has the advantage of three-dimensions (3D). The principle of XCT imaging has been extensively described elsewhere by Stock (18). In addition, the visual information has the potential to generate quantitative data. XCT has been employed to study spatial configurations, porosities and structures of soil (19), unstained soft biological tissues, and organic materials (20). The pharmaceutical industry has utilized microXCT to visualize the void network of large pharmaceutical granules (>1 mm) (21), measure density variations in pharmaceutical tablets (22) (20), and evaluate the particle size and shape distributions for mixtures of randomly packed particles (180–300 μm) (23). With the recent advent of the ultra high-resolution NanoXCT, microscopic samples can now be visualized in 3D, down to 2D spatial resolutions of 50 nm at a field of view of 16.6 μm. These settings make NanoXCT particularly suitable for characterizing individual pharmaceutical particles that may be a respirable size (24, 25).

This study aimed to demonstrate the novel application of NanoXCT in visualizing and quantifying the internal architecture of pharmaceutical particles. Various pharmaceutical particles (small molecules vs macromolecules) with different physicochemical properties (crystalline vs amorphous) were investigated. Macromolecules included a crystalline sugar (2-hydroxypropyl)-beta-cyclodextrin (HβCD) and an amorphous polymer poly (lactic-co-glycolic) acid (PLGA). Inhalable spray-dried formulations included smooth and nanomatrix bovine serum albumin (BSA) proteins, a lipid-based carrier, and crystalline mannitol.

MATERIALS AND METHODS

Materials

Raw HβCD, BSA (98% purity), and polyvinyl alcohol (PVA) (MW 31000–50000, 87–89% hydrolyzed) were purchased from Sigma-Aldrich, Castle Hill, Australia; PLGA (75:25, LACTEL Polymer) from Durect Corporation, Cupertino, United States; de-ionized water (electrical resistivity > 2MΩ cm at 25°C) was supplied by a Modulab Type II De-ionization System (Continental Water Systems, Sydney, Australia); all solvents were analytical grade from Thermo Fisher Scientific Australia Pty. Ltd., Scoresby, Australia.

Preparation of Particles

Raw HβCD

Raw HβCD, commercially available from Sigma-Aldrich (Castle Hill, Australia), was used as supplied.

PLGA

Blank PLGA microparticles were manufactured using a double emulsion method adapted from Kasturi *et al.* (26). Briefly, an aliquot of 0.5% w/v PVA in deionized water was homogenized at 7000 rpm (Unidrive ×1000, CAT Scientific, Paso Robles, United States) with a 10% w/v solution of PLGA in dichloromethane. This primary emulsion was then transferred to a 5% w/v PVA aqueous solution and homogenized again at the aforementioned parameters. The resulting double emulsion (w/o/w) was left under magnetic stirring (*MR Hei*-Standard Magnetic Stirrer, Heidolph Instruments, Schwabach, Germany) for four hours at room temperature to allow for solvent evaporation. The resulting PLGA microparticle suspension was subjected to centrifugation at 2000 g for 20 min (Minispin, Eppendorf, North Ryde, Australia) rinsed three times with deionized water, and then snap frozen in liquid nitrogen before freeze-drying (CHRIST Alpha 1–4, John Morris Scientific, Chatswood, Australia). Freeze-drying conditions were initially maintained at −25°C for 48 h and then at 20°C for 24 h.

Smooth BSA

Spray-dried BSA particles were prepared as described by Adi *et al.* (27) using a Büchi Mini Spray-Dryer B-290 (Büchi Labortechnik, Flawil, Switzerland) connected to a Büchi Dehumidifier B-296 operating at aspiration and atomization rates of 38 m^3/h and 819 Nl/h, respectively. An aqueous solution of BSA (60 mg/ml) was spray-dried at an inlet temperature of 55°C (outlet temperature of 38°C) and liquid feed rate of 2.4 ml/min.

Mannitol

Spray-dried mannitol was kindly supplied by Pharmaxis Ltd. (Frenchs Forest, Australia).

Nanomatrix

Nanomatrix BSA was produced by spray-drying a suspension containing primary nanoparticles of the protein as adapted from Kwok *et al.* (28). Primary nanoparticles were produced by an anti-solvent precipitation. Briefly, an aqueous solution of BSA (40 mg/ml) was rapidly poured into a volume of isopropanol (ratio of water to isopropanol was 3:7) in a 600 ml beaker stirred at 6000 rpm (Silverson Model L4RT high-shear mixer, Silverson Machines, Chesham, UK). The resulting suspension was diluted with ethanol to obtain a concentration of 4 mg/ml prior to spray-drying. The spray-dryer was operated with a Büchi B-295 Inert Loop and B-296 dehumidifier, and the operation conditions were: inlet temperature at 50°C (outlet temperature 35°C), liquid feed rate at 2.4 ml/min, aspiration at 38 m^3/h and atomization rate at 819 NL/h.

Lipid-Based Carriers

Lipid-based carriers were produced from an emulsion containing DSPC, $CaCl_2$, and PFOB (all purchased from Sigma Aldrich, Castle Hill, Australia) as previously described (29, 30). Briefly, the emulsion was homogenized using a high pressure homogenizer (Emulsiflex-C3, Avestin, Ottawa, Canada) and then spray dried using a custom bench-top spray-dryer (31) at settings similar to an inlet temperature of 100–110°C, outlet temperature 60–80°C, pump flow rate 31 ml/min, and gas flow 110 SCFM.

COLLOIDAL PROBE LOADING

Particles were mounted onto the sharp end of a tailor pin using a similar technique described by D'Sa *et al.* (32). Briefly, pins were temporarily mounted on a custom 70° angle holder and manipulated using a microscope stage (Olympus CX41, Notting Hill, Australia) to approach a glass slide containing epoxy (Hardman® Double-Bubble Epoxy, Carrum Downs, Australia), which was attached to the microscope lens casing *via* another custom holder. Particles were sampled from the bulk and sprinkled onto a separate microscope slide, and the same pin was then manipulated to approach a single particle or small agglomerate of interest on that slide.

Proper loading was verified by SEM (Zeiss Evo, Carl Zeiss Microscopy, Jena, Germany). Subsequently, a gold fiducial (1.5 - 3 μm diameter) (Alfa Aesar, Wardhill, USA) was attached on or near a particle of interest (Fig. 1) using a custom built manual micromanipulation apparatus fitted with 10× and 50× objectives and a video cross line generator (Boeckeler Inc, Model *Via*-30, Tucson AZ, USA). The gold fiducial is required to locate the particle of interest, calibrate the focus, and reconstruct the particle in 3D.

NANOXCT PARAMETERS AND SETUP

Depending on the size of the particle of interest, NanoXCT was operated in Zernike Phase Contrast (ZPC) mode and images were acquired using either: 1) large field of view (LFOV), which has a two-dimensional (2D) spatial resolution of 172 nm at a field of 65.5 μm in binning 1; or 2) high resolution (HRES) that has a respective resolution of 43.7 nm and a field of view of 16.6 μm in binning 1. The number of images scanned was based on binning, where a binning 1 required a minimum of 901 images. Scan times were chosen where the maximum signal detected had to be at least three times the value of the minimum detectable signal, resulting in a signal-to-noise ratio (S/N) of 3 to minimize background noise. While NanoXCT can also be operated in Absorption Contrast (AC) mode, preliminary scans for pharmaceutical materials showed that a PLGA particle was invisible in absorption compared with phase contrast imaging (Fig. 1). Therefore, only ZPC mode was used in the present study.

The NanoXCT setup is depicted in Fig. 2. The X-ray source is a Rigaku rotating copper anode that generates an 8 keV X-ray beam, which passes through a 5/10 μm Ni filter (5 for HRES, 10 for LFOV), a glass capillary condenser, and a 60/100/150 μm Ø pinhole before interacting with the rotating sample. The transmitted X-ray is then passed through a Fresnel zone plate and a phase ring before being collected by a 1024x1024 Charge-Coupled Detector (CCD).

IMAGE ANALYSIS

Reconstructed axial slice stacks of each scan were processed using Avizo Fire (FEI Visualization Sciences Group,

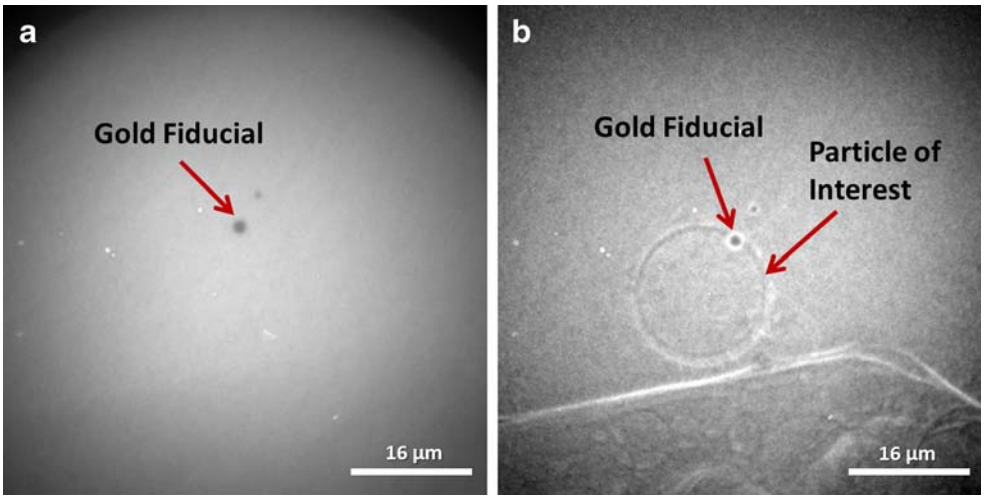

Fig. 1 Comparison of (**a**) absorption and (**b**) phase contrast imaging

Burlington, USA) in order to qualify and quantify physical characteristics. The slices were first subjected to a non-local means filtering to reduce noise contributions to the overall dataset. A binary mask based on density thresholding was generated from this filtered dataset to separate the regions of interest from the surrounding air to further minimize noise influences. A 3D watershed algorithm was then employed to separate the agglomeration into individual particles for further analysis (33). The algorithm is based on the assumption that eroding a binary image will cause features in contact to separate before they disappear (23). Subsequently, the void volume (includes pores and cavities) was defined as the difference between total volume of particle enclosed by a convex hull algorithm and the volume of solid material enclosed by a convex hull algorithm. The definition of solid material was based on a binarization of the data using a grey value (density) limit to determine the boundary between the solid and air. Finally, the void-to-material (%) was the ratio of void space to solid material given as a percentage.

RESULTS

Large Field of View

The larger sized raw HβCD and PLGA microparticles were acquired under LFOV mode. Cross-sectional NanoXCT images in Fig. 3A-C show that an HβCD particle contains various sized voids. Although these cross-sections are only snapshots of the particle at a specific location, when stacked together they produce a 3D representation of the whole HβCD particle (Fig. 3D). This 3D representation illustrates that the particle is comprised of several interconnected voids connected to the particle surface. In contrast, PLGA particles appeared to consist of a single large internal void (completely enclosed by the particle material) surrounded by a few much smaller voids. The large internal void is visible from the cross-sectional images, but is less apparent from the 3D representation since it is fully encompassed within the particle (Fig. 4). However, this internal void becomes visible in a sliced view of the 3D reconstruction Fig. 4D.

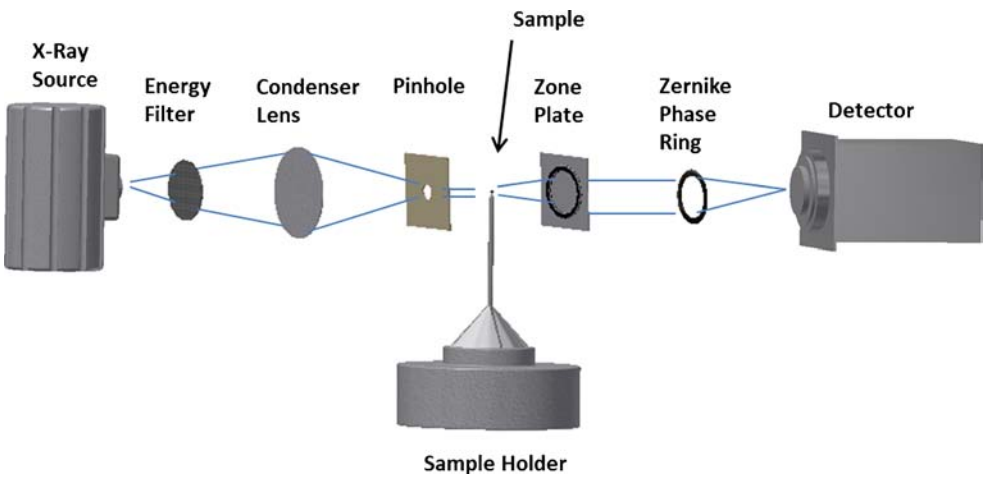

Fig. 2 Schematic of the NanoXCT. Diagram not drawn to scale

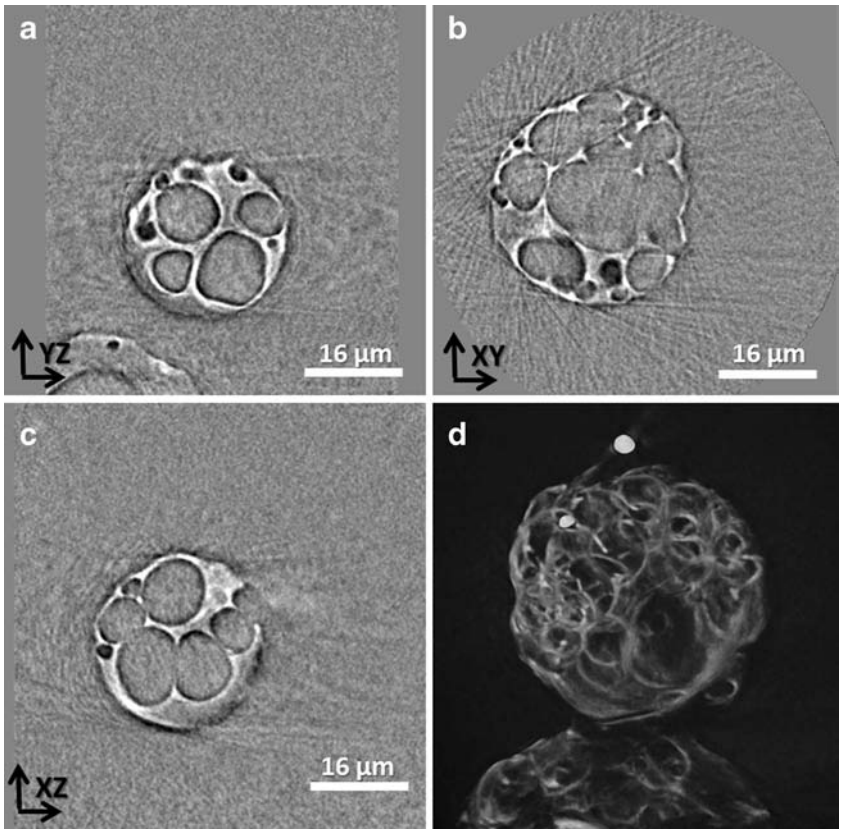

Fig. 3 NanoXCT images of an HβCD particle using LFOV: (**a**, **b**, **c**) cross-sectional images of the particle at various positions, and (**d**) reconstructed particle in 3D

High Resolution

The smaller sized spray-dried smooth and nanomatrix BSA, mannitol, and lipid-based carriers were acquired under HRES mode. NanoXCT revealed that smooth BSA particles were mostly solid or contained a single void (Fig. 5), which is in agreement with results reported by Heng *et al.* (8). In alignment with previous findings (8, 34), a large proportion of mannitol particles were porous (Fig. 6).

However, NanoXCT failed to obtain clear evaluations of highly porous lipid-based carriers (Fig. 7A & B) and nanomatrix BSA (Fig. 7C & D) due to the high noise-to-signal ratio and poor phase contrast. Regardless of the large background noise, NanoXCT still showed that lipid-based carriers had porous internal structures (Fig. 7A) similar to those found using TEM in a previous study (4). It is interesting to note that although TEM has a resolution of 50 pm, *versus* a spatial 2D resolution of 43.7 nm for NanoXCT in our studies, the previous study had comparable results to our findings. This highlights the challenge in producing images with clearly defined air-particle boundaries for samples that are less than 5 µm in diameter and have large void-to-material percentages.

The reconstructed 3D particles of all samples were also processed into videos showing the completed particles rotating 360° around an axis. These can be found in the supplementary materials.

Quantitative Analysis

Void volumes, void distributions, and void-to-material percentage of several ($n=23$) individual mannitol particles (Fig. 8) and a single PLGA particle (Fig. 9) were obtained using watershed-based segmentation and thresholding limits to differentiate between the material and enclosed air-filled voids. Spray-dried mannitol was found to have an average void volume of 0.117 ± 0.247 µm^3 and an average void-to-material percentage of 3.5%. On the other hand, the single PLGA particle had a void volume of 1993 µm^3 and void-to-material percentage of 59.3%.

DISCUSSION

NanoXCT was successfully used to visualize and quantify the internal architecture of various pharmaceutical particles. This study has reported the first series of non-destructive 3D visualizations of individual micron-sized particles, including those of a respirable size. The key factor that influences the quality of images obtained by the NanoXCT is the linear attenuation coefficient (LAC). The LAC is defined as the percent reduction in intensity per unit thickness of the material, and is related to the voltage of the X-ray beam, particle density and the atomic composition of the sample material. As the

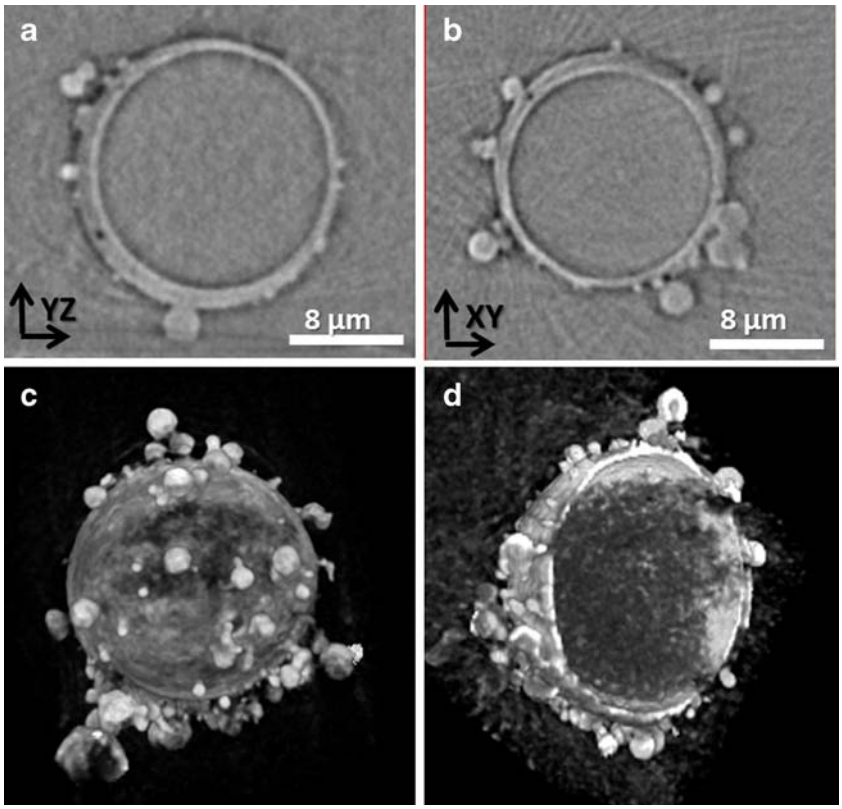

Fig. 4 NanoXCT images of a PLGA particle using LFOV: (**a**,**b**) cross-sectional images of the particle at various positions, (**c**) particle reconstructed in 3D, and (**d**) sliced view of the particle in 3D

X-ray voltage is fixed to 8 keV in the current setup, the LAC is most likely affected by porosity and the atomic composition of the sample. The porous internal structures of the lipid-based carriers and nanomatrix BSA (Fig. 7) meant these samples would have significantly lower LACs than a solid particle of the same material and size. As a result, there was minimal signal difference between the material of interest and background (air) so the particles appeared more transparent; making it difficult to distinguish between the particle and air boundaries. Alternatively, the atomic composition (a material specific property) can also play a role, in particular for the lipid-based carriers. Therefore, not all materials may be suitable for NanoXCT. While staining samples with agents such as osmium tetroxide may overcome this limitation, the staining process could introduce artifacts.

Another important factor is the size of the particle feature to be detected. With respect to the lipid-based carrier and nanomatrix BSA particles in Fig. 7, the particle features (*i.e.* the thin walls and primary size of the nanoparticles, respectively) approached the instrument resolution limit of 50 nm. In the case of nanomatrix BSA, even if adjacent nanoparticles are in contact, the void space would limit the signal that can be detected.

Instrument parameters that can be optimized to improve the imaging quality are binning, scan time, and number of images. The binning value determines the image resolution,

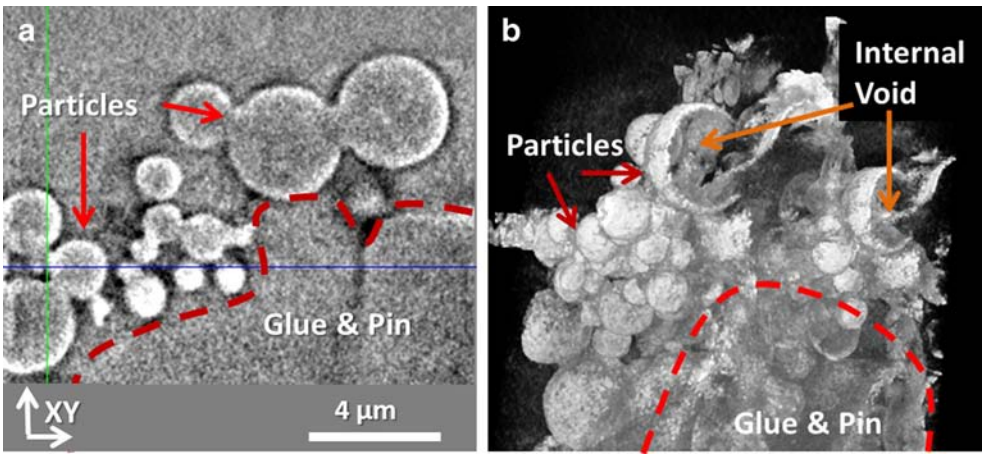

Fig. 5 NanoXCT images of smooth BSA particles using HRES: (**a**) cross-section and (**b**) particle reconstructed in 3D

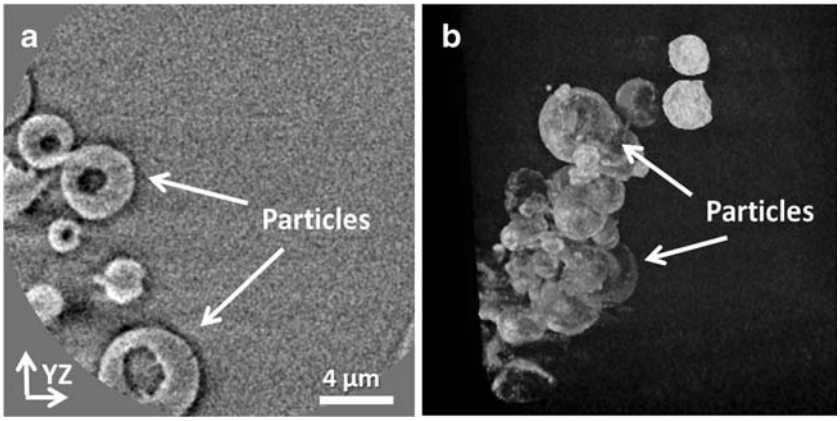

Fig. 6 NanoXCT images of mannitol particles using HRES: (**a**) cross-section and (**b**) particle reconstructed in 3D

where a value of 1 would provide the highest resolution. However, using lower binning values would decrease the maximal signal and increase background noise. Thus, the binning value chosen should be based on the resolution needed to detect the smallest feature. Another parameter is the scan time, which is the X-ray exposure time during a single image, and this affects image clarity. Longer scan times generally lead to greater signal and typically results in more defined material boundaries. Nonetheless, excessive scan times may not greatly improve the image quality so the minimum time that detects distinct material boundaries should be chosen. In addition, this instrument is not widely accessible and scans can take from one to four days, which can be costly and time-consuming. It is also important to note that the definition of particle boundaries is subjective and the data arising from overlapping areas could be a source of error. Nevertheless, this issue would apply to all microscopic techniques. Lastly, the number of images taken affects the clarity and precision of the 3D rendered image. Since 3D rendering software, such as Avizo Fire, extrapolates data between images, more images would reduce extrapolation gaps and produce a more precise 3D reconstruction.

Despite some of the limitations mentioned above, in comparison to existing advanced microscopic techniques, NanoXCT is the only non-destructive technique that offers 3D visualization. Although confocal microscopy is also capable of 3D visualization, when a material does not autofluoresce the process of labeling the feature of interest

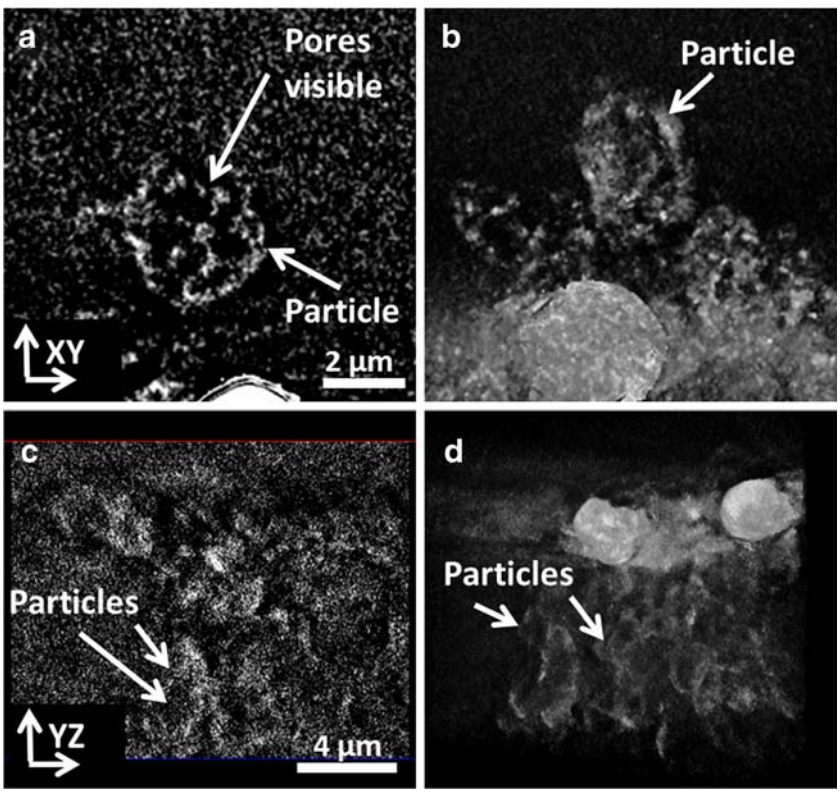

Fig. 7 NanoXCT images using HRES: (**a**) cross-section and (**b**) reconstructed particle in 3D of lipid-based carriers; (**c**) cross-section and (**d**) reconstructed particle in 3D of nano matrix bovine serum albumin (BSA)

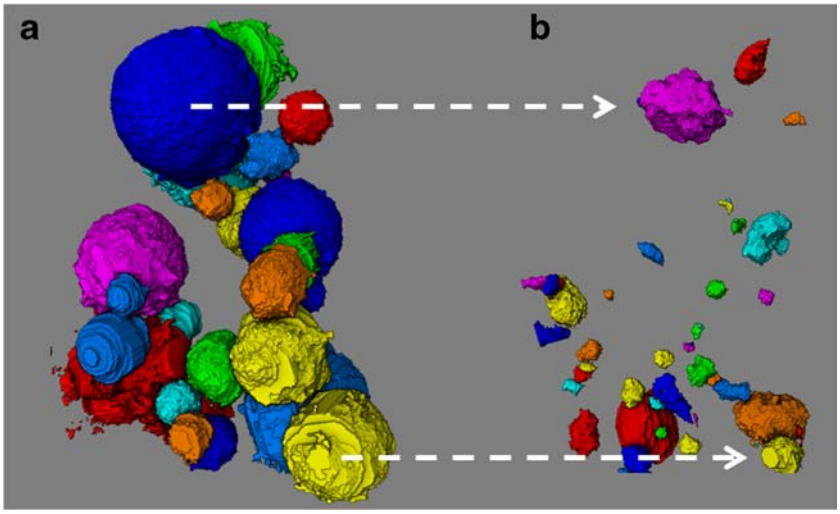

Fig. 8 Rendered 3D projections of mannitol particles: (**a**) identified using watershed-based segmentation and (**b**) voids located within particles

with a fluorophore could introduce artifacts. Other clear advantages of NanoXCT are that it requires little sample preparation; can be carried out under ambient conditions; the parameters do not need to be adjusted for different materials (though image quality may be improved by taking more images and using longer exposure times); it is possible to image multiple particles simultaneously within the field of view; and the method does not require the operator to be present throughout the scan, which enables efficient collection of data.

In addition, NanoXCT can go beyond pure visualization to extract quantitative information (35–38). The literature has shown that NanoXCT is an accurate and sensitive measure for quantitative imaging, segmentation, and identification of different phases in complex materials at the nanoscale (35). The quantitative capabilities have been demonstrated in systems such as aggregated 165 nm polystyrene particles (38), cartilage subtissues and bone architectures (37, 39), SiO_2 microparticles (35), flocculated clay suspensions, and cement pastes (36); but our study is the first to report quantitative findings in pharmaceutical particles. Our results show the first examples of the use of NanoXCT to quantify void volumes, void distributions, and void-to-material percentages.

Similar to FIB-SEM, NanoXCT may also be used to correlate aerodynamic properties with porosity to explain the performance of specific formulations. While FIB-SEM has been a relatively robust method, evaluation of porosity has been limited to the number of particles with porous interiors (8). Since NanoXCT reconstructs volume, the

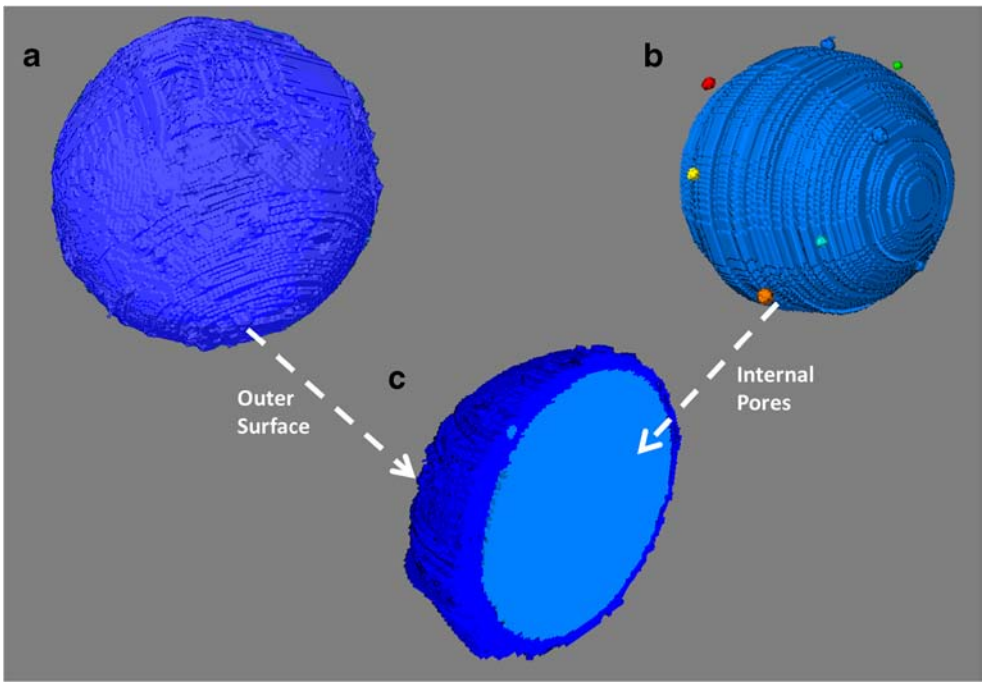

Fig. 9 Rendered 3D projections of a PLGA particle: (**a**) particle outline, (**b**) voids located within the particle, and (**c**) sliced view of the entire particle

quantification of void volumes, void distributions and void-to-material percentages may be more accurate. The application of NanoXCT as an analytical tool is not confined to respirable particles only. For example, the density (inversely related to the porosity) of a formulation can be a measure of physical stability (40); it may determine flow properties as well as release/dissolution rates from dosage forms administered orally, parentally, rectally and topically. Hence, the insight offered by NanoXCT into sample porosity could have important implications on the processing and manufacturing of pharmaceuticals.

Overall, the 3D visual capability provides full access to the internal structures of small pharmaceutical particles. This novel technique opens up opportunities to characterize particles in greater detail and future studies will use NanoXCT to identify different components in a mixture (*i.e.* physical mixtures and co-spray dried formulations) as well as compare the quantitative capabilities of NanoXCT to other advanced microscopic techniques. Another study will also attempt to use this tool to explain aerosol performance of a specific particle formulation.

CONCLUSIONS

NanoXCT presents a powerful tool to dissect and observe the interior of small pharmaceutical particles, including those of an inhalable size. It provided valuable insight into the void volumes, void distributions, and void-to-material percentages. Other advanced microscopic techniques (confocal microscopy, SEM, TEM, and FIB) may complement NanoXCT to obtain a more complete picture of a particle of interest and enable aerosol scientists to better explain its aerodynamic behaviour.

ACKNOWLEDGMENTS AND DISCLOSURES

Jennifer Wong and Dexter D'Sa contributed equally to this work.

The authors acknowledge the facilities and technical assistance of Steve Moody (SEM and FIB Specialist) and the Australian Microscopy & Microanalysis Research Facility at the Australian Centre for Microscopy & Microanalysis, University of Sydney. Jennifer Wong, Dexter D'Sa and John Chan were recipients of the Australian Postgraduate Award, and Dexter D'Sa was also the recipient of the Australian IPRS scholarship. This work was supported under the Australian Research Council"s *Discovery Projects* funding scheme (projects DP120102778 & 110105161).

SUPPLEMENTARY MATERIAL

A video showing the reconstructed 3D particles of all samples rotating 360° around an axis can be found in the supplementary materials.

REFERENCES

1. Chow AHL, Tong HHY, Chattopadhyay P, Shekunov BY. Particle engineering for pulmonary drug delivery. Pharm Res. 2007;24:411–37.
2. Vehring R, Lechuga-Ballesteros D, Joshi V, Noga B, Dwivedi SK. Cosuspensions of microcrystals and engineered microparticles for uniform and efficient delivery of respiratory therapeutics from pressurized metered dose inhalers. Langmuir. 2012;28:15015–23.
3. Vanbever R, Mintzes J, Wang J, Nice J, Chen D, Batycky R, *et al.* Formulation and physical characterization of large porous particles for inhalation. Pharm Res. 1999;16:1735–42.
4. Dellamary LA, Tarara TE, Smith DJ, Woelk CH, Adractas A, Costello ML, *et al.* Hollow porous particles in metered dose inhalers. Pharm Res. 2000;17:168–74.
5. Crowder TM, Rosati JA, Schroeter JD, Hickey AJ, Martonen TB. Fundamental effects of particle morphology on lung delivery: Predictions of Stoke's law and the particular relevance to dry powder inhaler formulation and development. Pharm Res. 2002;19:239–45.
6. D'Addio SM, Chan JGY, Kwok PCL, Prud'homme RK, Chan H-K. Constant size, variable density aerosol particles by ultrasonic spray freeze drying. Int J Pharm. 2012;427:185–91.
7. Chew NYK, Tang P, Chan H-K, Raper JA. How much particle surface corrugation is sufficient to improve aerosol performance of powders? Pharm Res. 22:148–152 (2005).
8. Heng D, Tang P, Cairney J, Chan H-K, Cutler D, Salama R, *et al.* Focused-ion-beam milling: A novel approach to probing the interior of particles used for inhalation aerosols. Pharm Res. 2007;24:1608–17.
9. Chew NYK, Chan H-K. Influence of particle size, air flow, and inhaler device on the dispersion of mannitol powders as aerosols. Pharm Res. 1999;16:1098–103.
10. Chew NYK, Chan H-K. Use of solid corrugated particles to enhance powder aerosol performance. Pharm Res. 2001;18:1570–7.
11. Chiou H, Chan H-K, Heng D, Prud'homme RK, Raper JA. A novel production method for inhalable cyclosporine A powders by confined liquid impinging jet precipitation. J Aerosol Sci. 2008;39:500–509.
12. Zhu B, Traini D, Chan H-K, Young PM. The effect of ethanol on the formation and physico-chemical properties of particles generated from budesonide solution-based pressurized metered-dose inhalers. Drug Dev Ind Pharm. 2013;39:1625–37.
13. Larson D, Foord D, Petford-Long A, Anthony T, Rozdilsky I, Cerezo A, *et al.* Focused ion-beam milling for field-ion specimen preparation: Preliminary investigations. Ultramicroscopy. 1998;75:147–59.
14. Miller MK, Russell KF, Thompson K, Alvis R, Larson DJ. Review of atom probe FIB-based specimen preparation methods. Microsc Microanal. 2007;13:428–36.
15. Vieu C, Gierak J, Launois H, Aign T, Meyer P, Jamet J, *et al.* High resolution magnetic patterning using focused ion beam irradiation. Microelectron Eng. 2000;53:191–4.
16. Fu Y, Bryan NKA, Shing O, Hung N. Influence of the redeposition effect for focused ion beam 3D micromachining in silicon. Int J Adv Manuf Technol. 2000;16:877–80.
17. Shurand J, Price R. Advanced microscopy techniques to assess solid-state properties of inhalation medicines. Adv Drug Deliv Rev. 2012;64:369–82.
18. Ketchamand RA, Carlson WD. Acquisition, optimization and interpretation of X-ray computed tomographic imagery: Applications to the geosciences. Comput Geosci. 2001;27:381–400.
19. Taina I, Heck R, Elliot T. Application of X-ray computed tomography to soil science: A literature review. Can J Soil Sci. 2008;88:1–19.
20. Momose A, Takeda T, Itai Y, Hirano K. Phase–contrast X–ray computed tomography for observing biological soft tissues. Nat Med. 1996;2:473–5.

21. Farber L, Tardos G, Michaels JN. Use of X-ray tomography to study the porosity and morphology of granules. Powder Technol. 2003;132:57–63.
22. Sinka IC, Burch SF, Tweed JH, Cunningham JC. Measurement of density variations in tablets using X-ray computed tomography. Int J Pharm. 2004;271:215–24.
23. Fu X, Dutt M, Bentham AC, Hancock BC, Cameron RE, Elliott JA. Investigation of particle packing in model pharmaceutical powders using X-ray microtomography and discrete element method. Powder Technol. 2006;167:134–40.
24. Attwood D. Microscopy: Nanotomography comes of age. Nature. 2006;442:642–3.
25. Sakdinawatand A, Attwood D. Nanoscale X-ray imaging Nature Photonics. 2010;4:840–8.
26. Kasturi SP, Skountzou I, Albrecht RA, Koutsonanos D, Hua T, Nakaya HI, *et al.* Programming the magnitude and persistence of antibody responses with innate immunity. Nature. 2011;470:543–7.
27. Adi S, Adi H, Tang P, Traini D, Chan H-K, Young PM. Microparticle corrugation, adhesion and inhalation aerosol efficiency. Eur J Pharm Sci. 2008;35:12–8.
28. Kwok P, Tunsirikongkon A, Glover W, Chan H-K. Formation of protein nano-matrix particles with controlled surface architecture for respiratory drug delivery. Pharm Res. 2011;28:788–96.
29. Tarara TE, Hartman MS, Gill H, Kennedy AA, Weers JG. Characterization of suspension-based metered dose inhaler formulations composed of spray-dried budesonide microcrystals dispersed in HFA-134a. Pharm Res. 2004;21:1607–14.
30. Weers JG, Tarara TE, Gill H, English BS, Dellamary LA. Homodispersion technology for HFA suspensions: particle engineering to reduce dosing variance. Respiratory Drug Delivery. 2000;2:91–7.
31. Iveyand JW, Vehring R. The use of modeling in spray drying of emulsions and suspensions accelerates formulation and process development. Comput Chem Eng. 2010;34:1036–40.
32. D'Sa D, Chan H-K, Chrzanowski W. Attachment of micro- and nano-particles on tipless cantilevers for colloidal probe microscopy. J Colloid Interface Sci (2014).
33. Russ JC. The Image Processing Handbook. London: Boca Raton; 1995.
34. Elverssonand J, Millqvist-Fureby A. Particle size and density in spray drying — Effects of carbohydrate properties. J Pharm Sci. 2005;94:2049–60.
35. Diaz A, Trtik P, Guizar-Sicairos M, Menzel A, Thibault P, Bunk O. Quantitative X-ray phase nanotomography. Phys Rev B. 2012;85:020104.
36. Brisard S, Chae RS, Bihannic I, Michot L, Guttmann P, Thieme J, *et al.* Morphological quantification of hierarchical geomaterials by X-ray nano-CT bridges the gap from nano to micro length scales. Am Mineral. 2012;97:480–3.
37. Dong P, Pacureanu A, Zuluaga MA, Olivier C, Frouin F, Grimal Q, Peyrin F. A new quantitative approach for estimating bone cell connections from nano-CT images, Engineering in Medicine and Biology Society (EMBC), 2013 35th Annual International Conference of the IEEE, 2013, pp. 3694–3697.
38. Trtik P, Soos M, Münch B, Lamprou A, Mokso R, Stampanoni M. Quantification of a single aggregate inner porosity and pore accessibility using hard X-ray phase-contrast nanotomography. Langmuir. 2011;27:12788–91.
39. Kerckhofs G, Sainz J, Wevers M, Van de Putte T, Schrooten J. Contrast-enhanced nanofocus computed tomography images the cartilage subtissue architecture in three dimensions. Eur Cell Mater. 2013;25:179–89.
40. D'Sa D, Chan H-K, Chrzanowski W. Predicting physical stability in pressurized metered dose inhalers *via* dwell and instantaneous force colloidal probe microscopy. Eur J Pharm Sci (Submitted).